Supplementary information for

Singularity-free supertwisted atomic layers with giant circular dichroisms

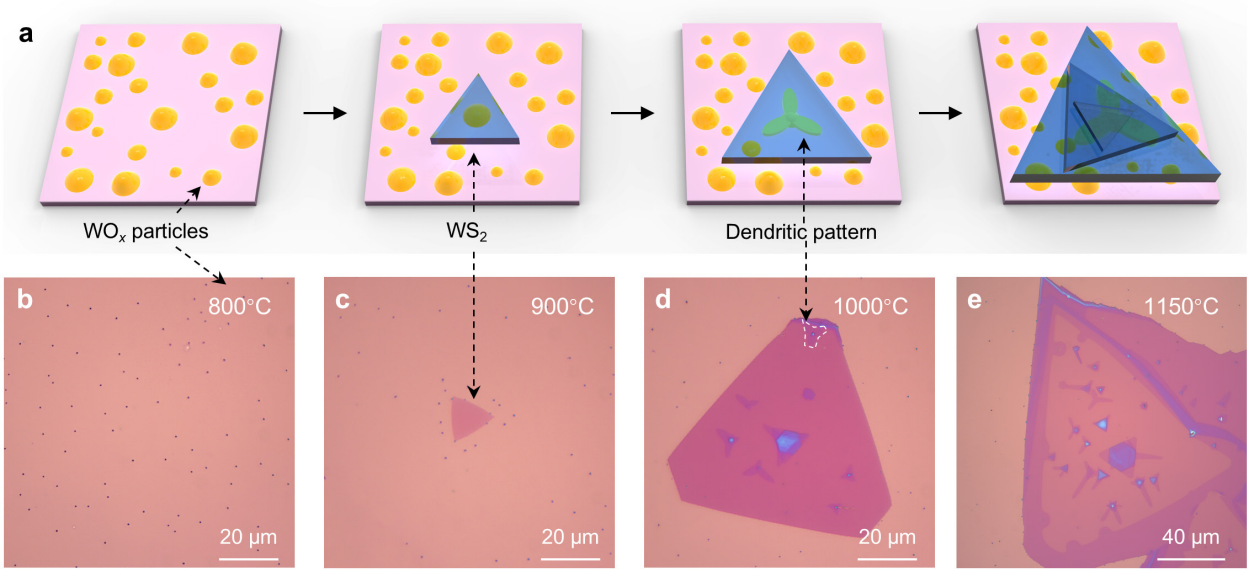
Xinchao Wang, Kaifeng Lin, Guodong Xue, Lifeng Hou, Yinghui Wei, Liantuan Xiao, Hao Hong, Xiaopeng Fan and Kaihui Liu

This PDF file includes:

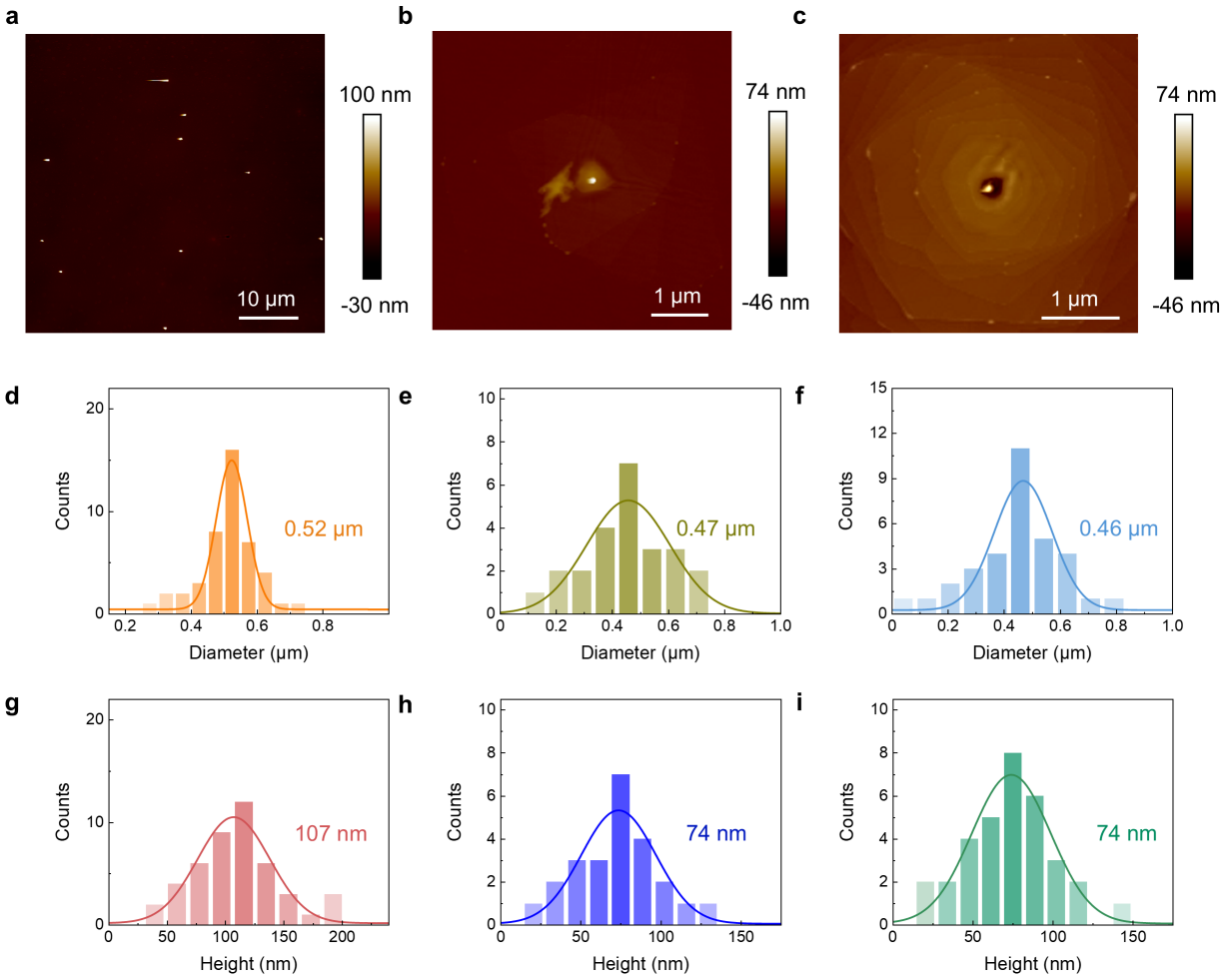
Supplementary Figures 1-16

Supplementary Note 1, 2

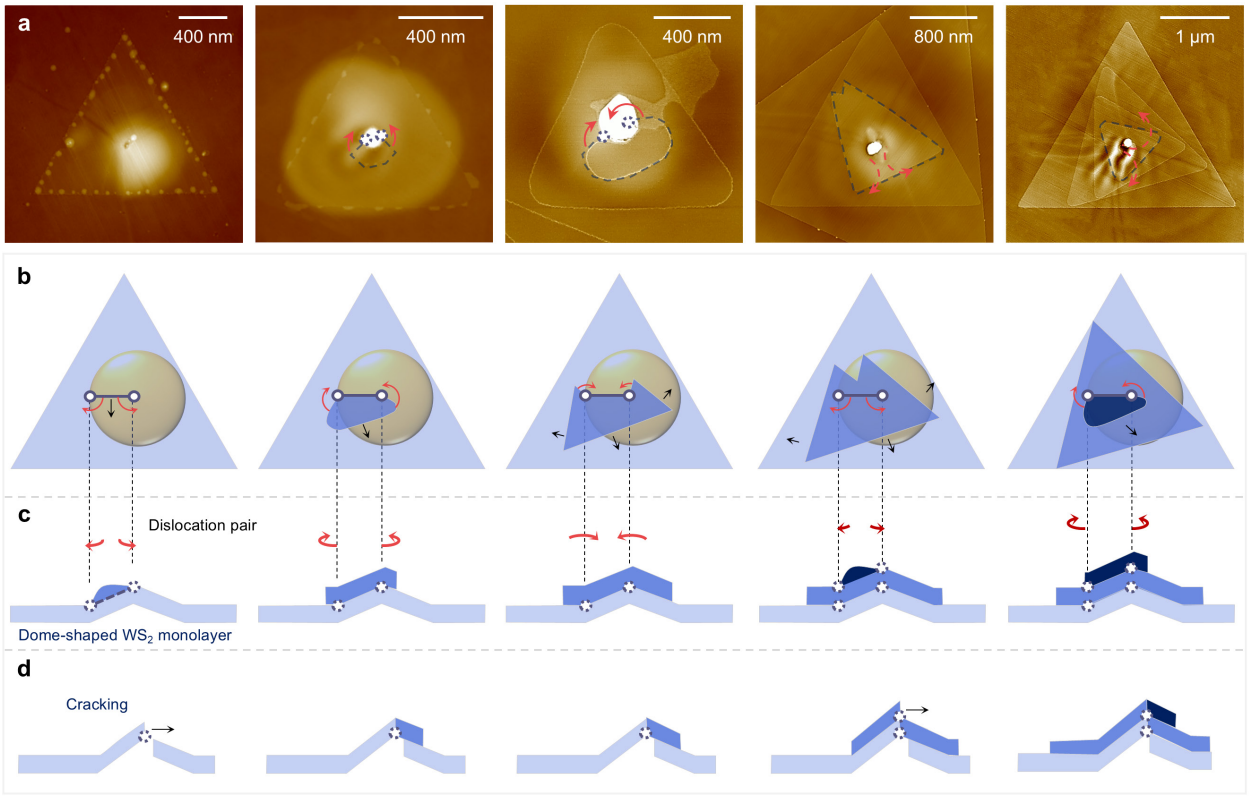
Supplementary References



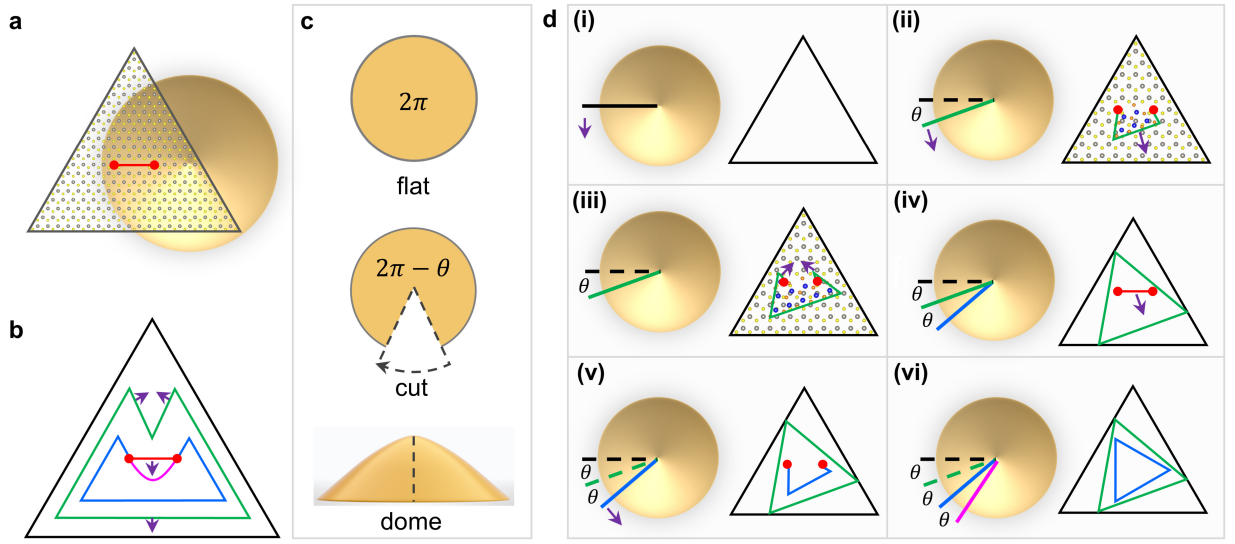
Supplementary Figure 1 | Schematic illustration and experimental evidence of the growth process. a, Schematic illustration of the growth process. **b,** Optical image of WO_x nanoparticles on the Si/SiO_2 substrate after growth interruption at 800°C. **c,** Optical image of monolayer WS_2 obtained after growth interruption at 900°C. The monolayer WS_2 expands and partially coats the nanoparticles. **d,** Optical image showing further expansion of monolayer WS_2 after growth interruption at 1000°C. The white dashed line outlines the dendritic pattern formed underneath the monolayer WS_2. **e,** Optical image of few-layer WS_2 structures grown at 1150°C for 3 min. Dendritic patterns are observed beneath nearly all few-layer structures. Supplementary figure 1a was created using Blender 5.1 (https://www.blender.org/).



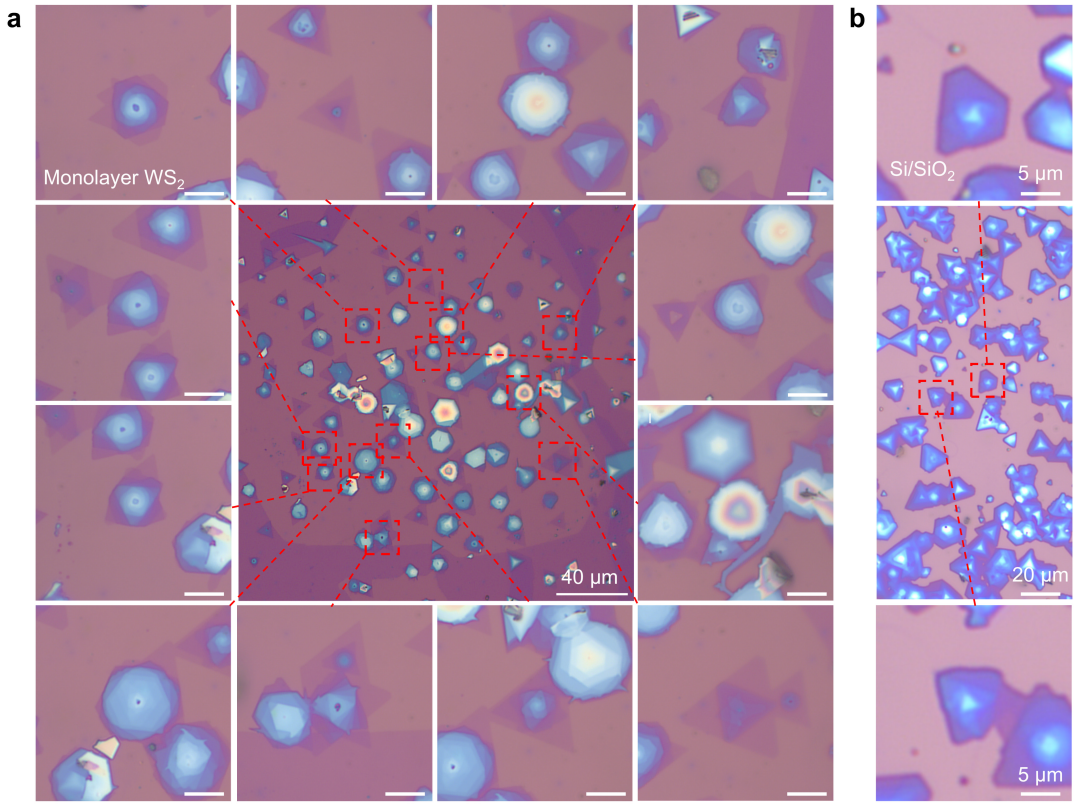
Supplementary Figure 2 | Comparison of dome structure parameters at different growth stages under identical experimental conditions. a, AFM image of WO_x nanoparticles on the Si/SiO_2 substrate after growth interruption at 800°C. **b,** AFM image of few-layer WS_2 structures grown at 1150°C for 3 min. **c,** AFM image of supertwisted WS_2 multilayers grown at 1150°C for 10 min. **d–f,** Diameter distributions of nanoparticles and dome structures at the corresponding stages shown in (a–c). **g–i,** Height distributions of nanoparticles and dome structures at the corresponding stages shown in (a–c).



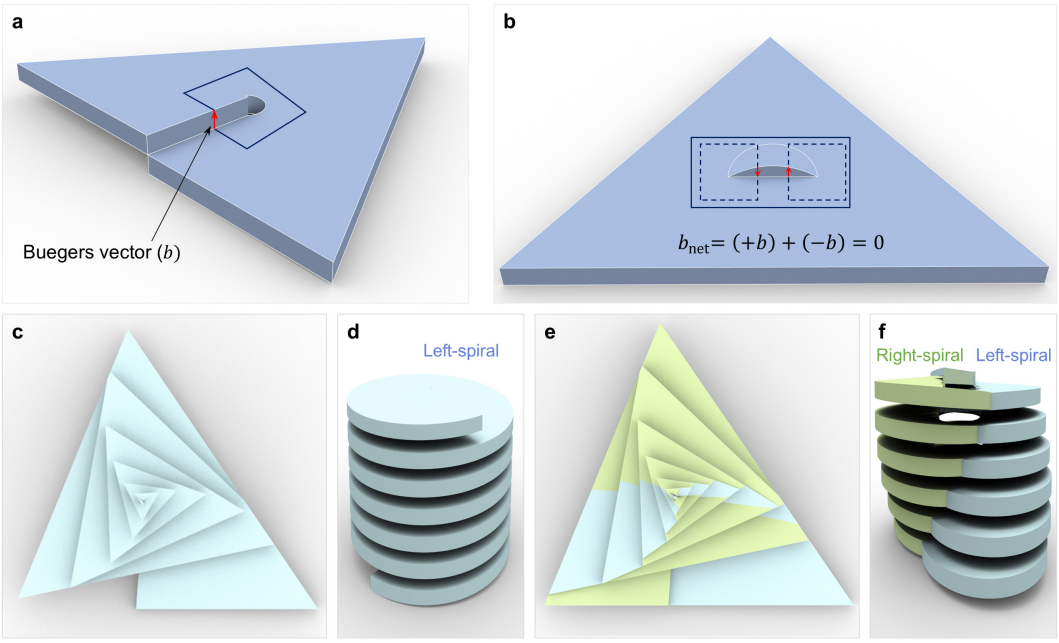
Supplementary Figure 3 | Growth mechanism driven by a crack line on a dome-shaped WS_2 monolayer. a, Typical AFM images showing different growth stages driven by a conjugate pair of screw- dislocations. **b–d,** Corresponding schematics showing the top view (b), front view (c), and side view (d). Red and black arrows indicate the growth direction of the dislocation pair and the layer extension direction, respectively.



Supplementary Figure 4 | Schematic illustrations of the formation of identical interlayer twist angles in singularity-free supertwisted WS_2. a, Spatial position of a dislocation line (red line) is located on the WS_2 dome. (Gray spheres: W atoms; yellow spheres: S atoms). **b,** Growth mechanism of a Frank–Read source on planar substrates. **c,** A dome structure can be constructed by removing a sector with an angular deficit θ from a planar sheet and joining the cut edges. **d,** Schematic of the formation of the uniform interlayer twist angles. **i,** A representative relative positional relationship between Frank–Read source and vdW dome. The purple arrows indicate the direction of growth. **ii,** Owing to the angular deficit of the dome structure, the initial lattice orientation at the Frank–Read dislocation source deviates from the black dashed line, forming an angle θ, as indicated by the green line. **iii–iv,** The second-layer edge, depicted in green, encircles pinning points to form a new WS_2 layer and a Frank–Read source. Note the angle θ between the lattice orientation at the dislocation (blue) and the second-layer lattice orientations. **v–vi,** This process repeats iteratively, with an angle θ present between the lattice orientation at the dislocation (purple line) and the lattice orientation of the third layer (blue line). The atomic models in this figure were produced using VESTA[1].

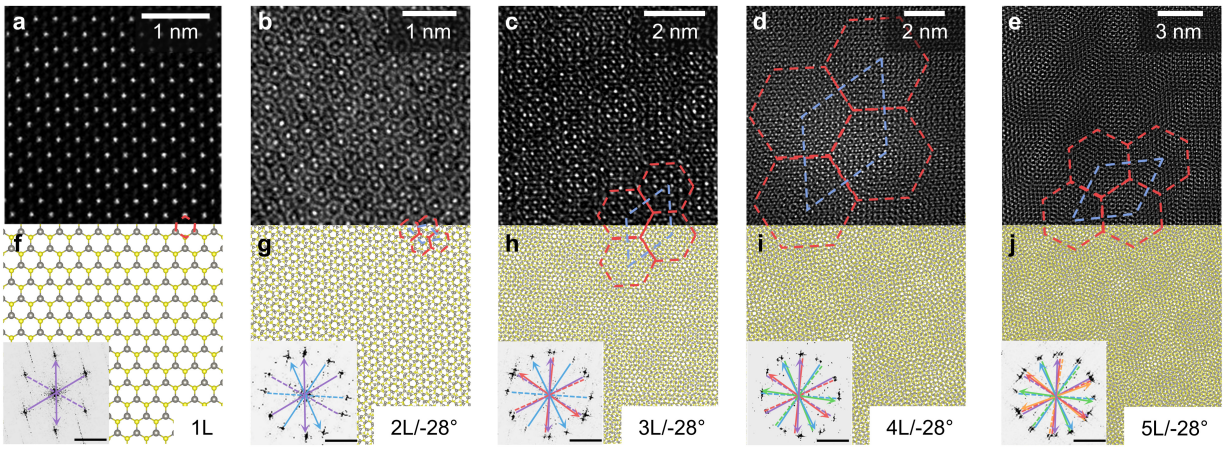


Supplementary Figure 5 | Optical images of singularity-free supertwisted multilayers and supertwisted spirals. a, Supertwisted multilayers grown on monolayer WS_2. Scale bars: 7 μm. **b,** Supertwisted spirals grown on a Si/SiO_2 substrate.

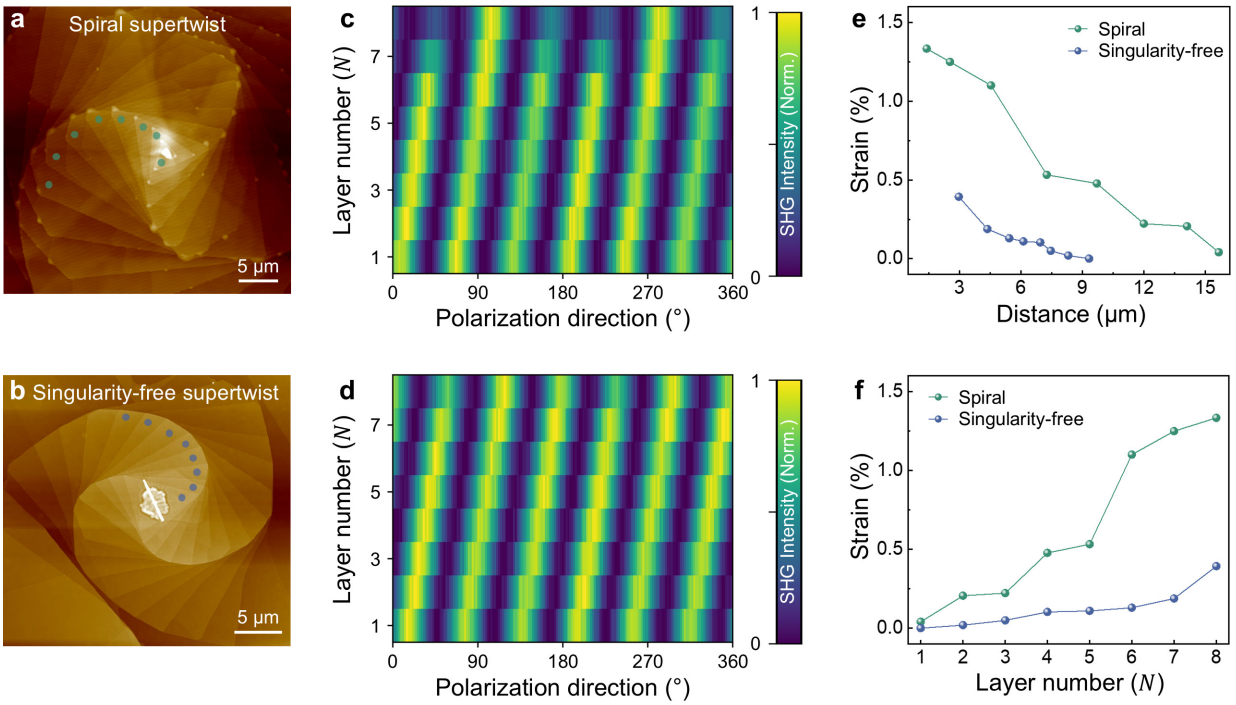


Supplementary Figure 6 | Structural comparison between the singularity-free supertwisted multilayer and supertwisted spiral. a, Burgers circuit encircling a single screw dislocation. **b,** Burgers circuit encircling the entire crack line. **c,** Schematic of a supertwisted spiral. **d,** Schematic of the single screw dislocation in the supertwisted spiral. **e,** Schematic of a singularity-free supertwisted multilayer, in which growth is driven by a conjugate pair of opposite-handed screw dislocations at the two termini of a crack line. **f,** Schematic of the crack-line region in the singularity-free supertwisted multilayer. Supplementary figure 6 was created using Blender 5.1 (https://www.blender.org/).

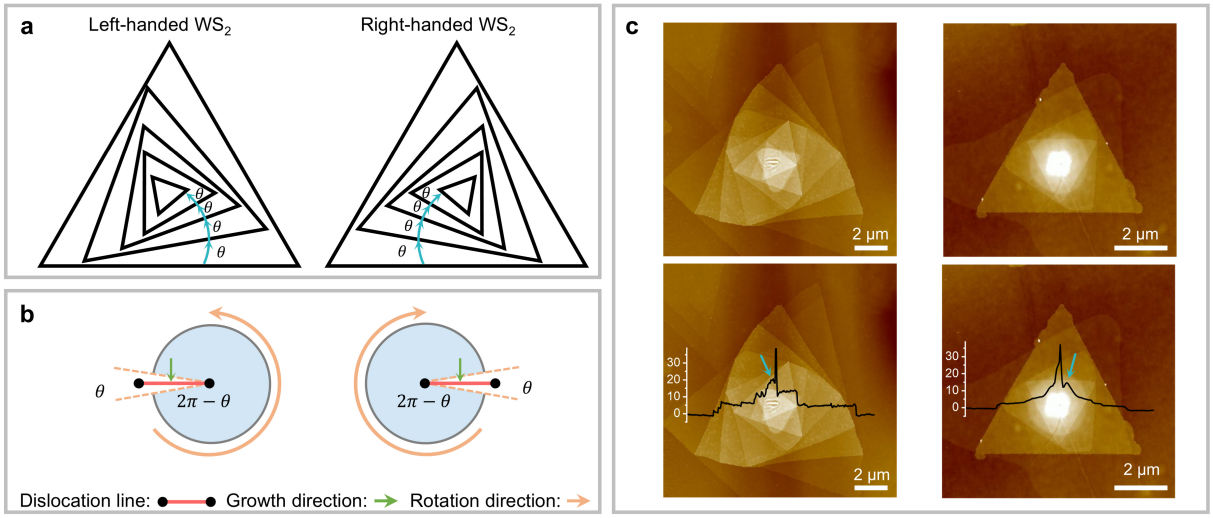
Here, Singularity-free is defined based on the net Burgers vector of the entire defect system: when all defects are enclosed by a Burgers circuit, the resulting net Burgers vector is zero ($b_{\text{net}} = 0$). This condition indicates the absence of a net topological singularity, but does not imply that the structure is completely defect-free. The crack line can be regarded as a pair of screw dislocations with opposite Burgers vectors, $+b$ and $-b$, located at its two termini. The net Burgers vector is therefore zero ($b_{\text{net}} = (+b) + (-b) = 0$). As a result, growth does not proceed as a continuous spiral around a single dislocation core; instead, two opposite-handed growth fronts generated from the crack-line region coalesce to form closed triangular loops.



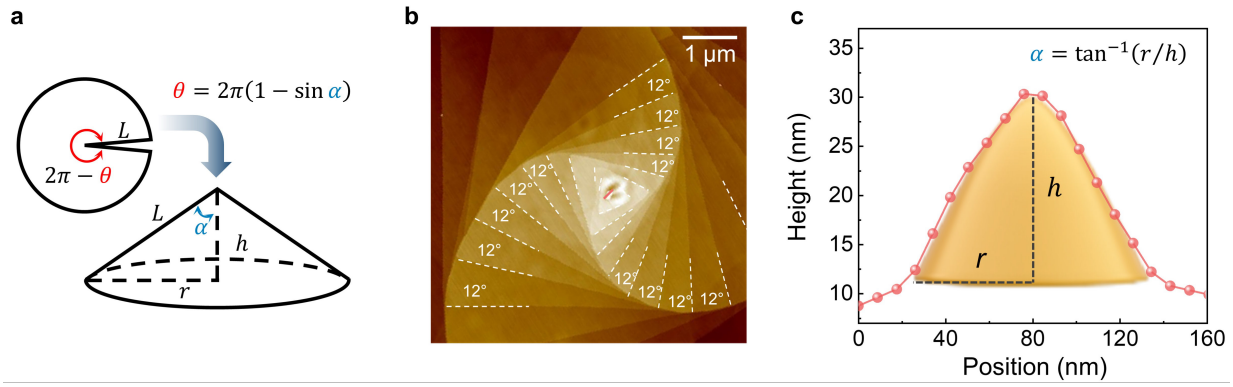
Supplementary Figure 7 | Atomic resolution HAADF-STEM images of 28° supertwisted WS_2 from one to five layers. a–e, High-resolution HAADF images collected from the one-, two-, three-, four- and five-layer areas. **f–j,** Simulated moiré patterns corresponding to (a–e) using WS_2 models (W atoms, gray balls; S atoms, yellow balls). STEM results and the simulated model are highly consistent and fit together well. The insets in (f–j) show the corresponding SAED pattern in (a–e). Scale bars: 3 nm^{-1}. The atomic models in this figure were produced using VESTA[1].



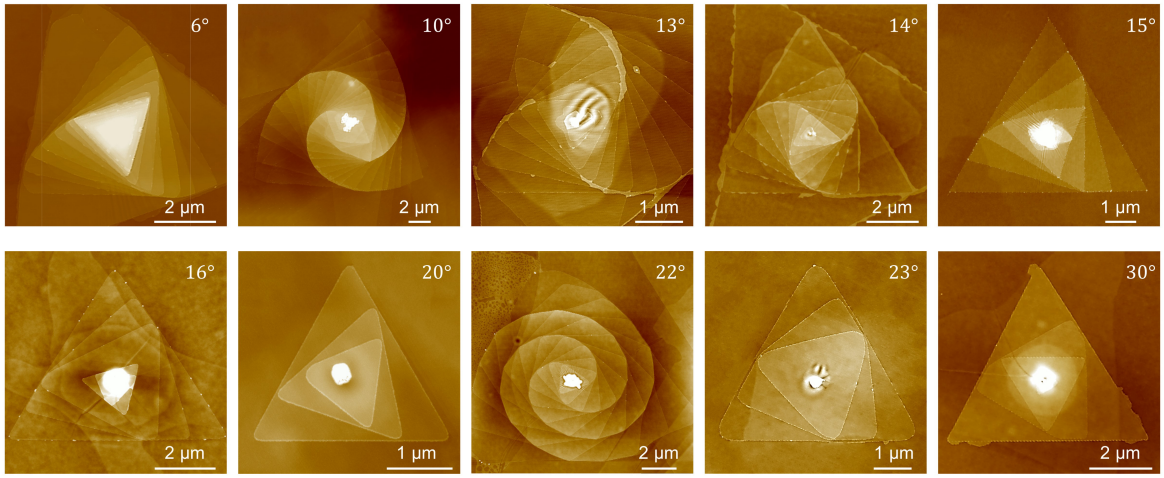
Supplementary Figure 8 | Strain comparison between spiral and singularity-free supertwisted multilayers. a, b, AFM images of a spiral supertwist and a singularity-free supertwist, with interlayer twist angles of $+12°$ and $-12°$, respectively. The green and blue circles mark the centers of the optical spots used for polarization-resolved SHG measurements. **c, d,** Layer-resolved polarization-dependent SHG intensity maps for the spiral and singularity-free supertwists, respectively. The SHG intensity of each layer is normalized independently. **e, f,** Strain extracted by fitting the polarization-dependent SHG patterns in (c) and (d), plotted as a function of distance from the twist centre and layer number, respectively. The singularity-free supertwist shows substantially reduced strain compared with the spiral supertwist.



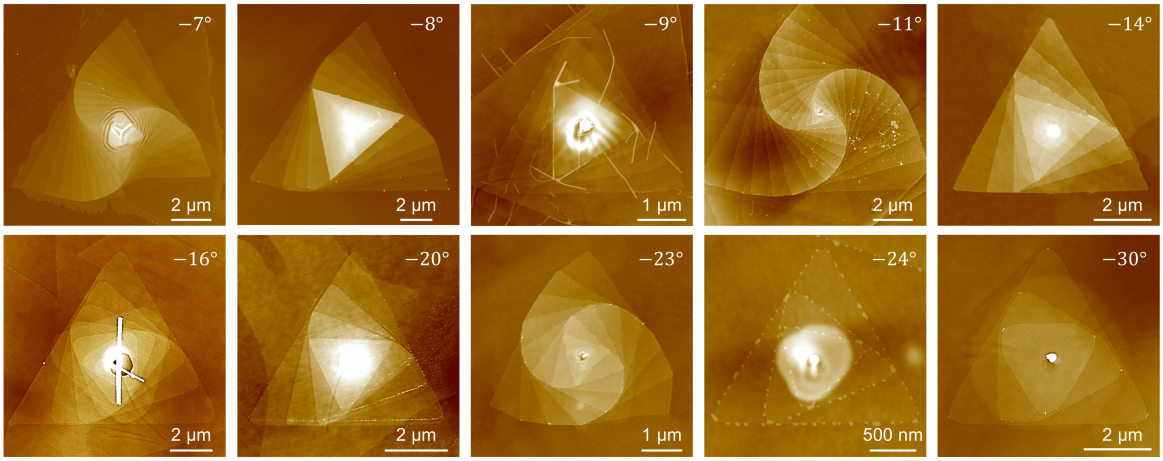
Supplementary Figure 9 | Tuneable chirality of supertwisted WS_2 multilayers. a, Schematic diagrams of left-handed and right-handed supertwisted WS_2 multilayer models. **b,** Schematic diagrams of the projections of vdW domes onto a plane. A dislocation line situated on the left side of the dome produces a left-handed chiral structure, whereas a line on the right side yields a right-handed chiral structure. **c,** AFM images of right- and left-handed WS_2 multilayers. The height profiles provide evidence for right- and left-handed WS_2 multilayers.



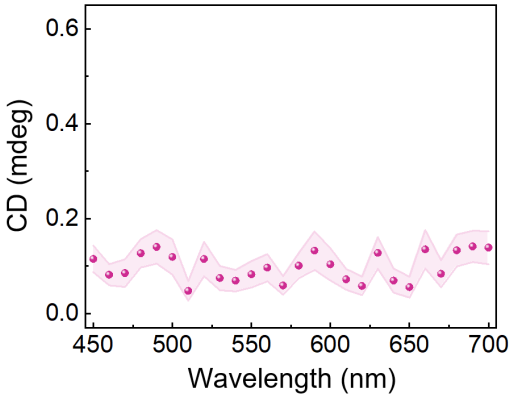
Supplementary Figure 10 | Twist angle control of supertwisted WS_2 multilayers. a, Schematic illustrates the process of folding a sector to form a dome structure. Experimentally, the twist angle of the multilayers can be modulated by changing the half-apex angle of the dome structure. **b,** AFM image of a supertwisted WS_2 multilayers. The interlayer twist angle is stabilized at 12° obtained from three directions through the step edges. **c,** Approximate height information obtained for the conical surface. The theoretically calculated twist angle of 12.46° matches the actual.



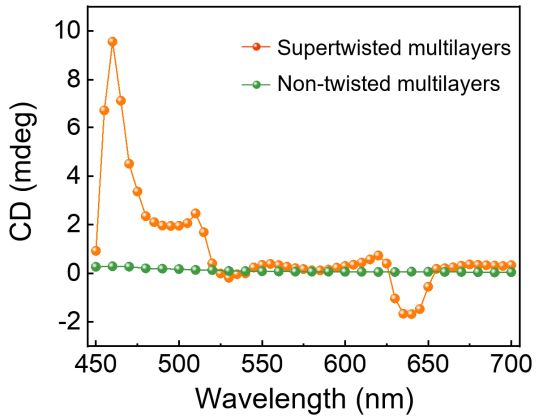
Supplementary Figure 11 | AFM images of the right-handed WS_2 with the twist angles increasing from 6°-30°.



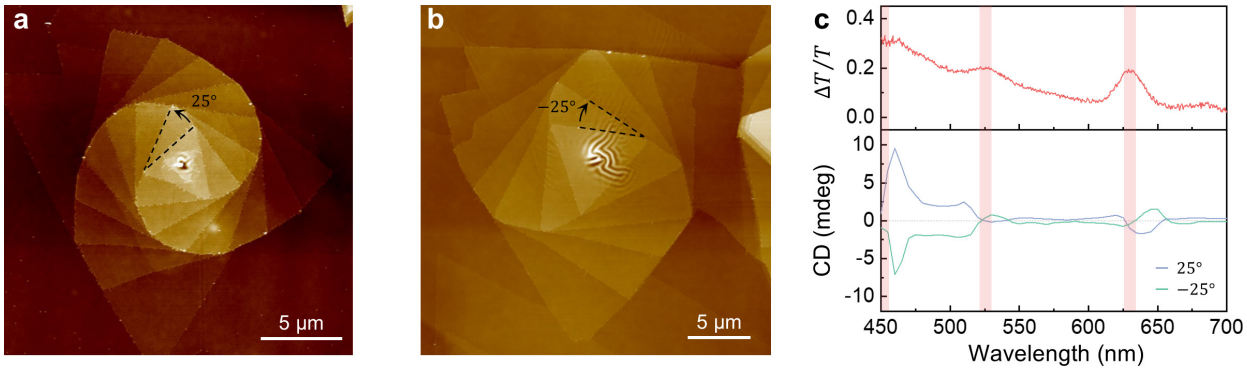
Supplementary Figure 12 | AFM images of the left-handed WS_2 with the twist angles increasing from 7°-30°.



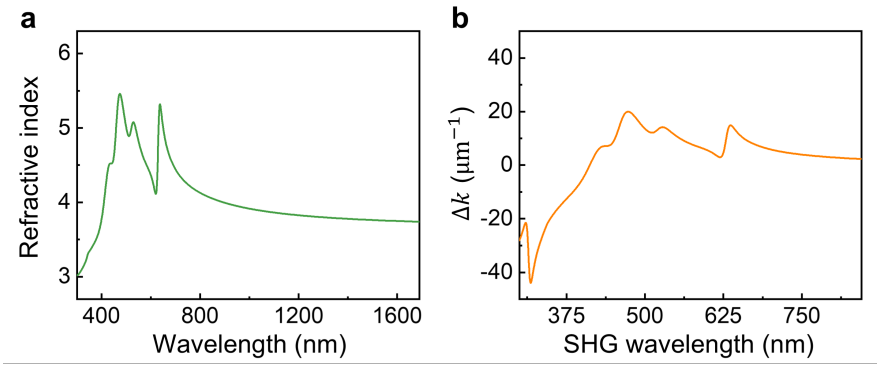
Supplementary Figure 13 | Circular dichroism of the fused silica substrate. Wavelength-dependent circular dichroism (CD) measured from the fused silica substrate using the same optical setup as that used for the supertwisted WS_2 samples. The substrate exhibits a weak CD response across the measured spectral range. The pink shaded region represents the error bar.



Supplementary Figure 14 | Comparison of linear CD between non-twisted and supertwisted samples. Linear circular dichroism spectra of non-twisted and supertwisted multilayer samples. The green curve, plotted against the left axis, represents the non-twisted multilayers and shows only a weak CD response. The orange curve, plotted against the right axis, represents the supertwisted multilayers and exhibits a much stronger CD signal.



Supplementary Figure 15 | A direct comparison of both enantiomers. a, AFM image of the original supertwisted WS_2 sample in Fig. 3 of the original manuscript. **b,** AFM image of the angle-symmetric enantiomeric sample. **c,** Differential transmission spectrum ($\Delta T/T$), of the original sample (top) and linear-absorption circular dichroism (CD) spectra of the two enantiomeric samples (bottom). The blue and green curves correspond to the original sample and the newly identified enantiomer, respectively.



Supplementary Figure 16 | Refractive index dispersion curve and wave vector difference (Δk) at different wavelengths. a, Dispersion of the refractive index for WS_2[2]. **b,** Δk of WS_2 at different wavelengths.

Supplementary Note 1: Numerical Kramers–Kronig transformation from experimental circular dichroism to optical rotatory dispersion

To obtain the optical rotatory dispersion (ORD) spectrum from experimentally measured CD data, a numerical Kramers–Kronig (KK) transformation was employed. The transformation exploits the fundamental causality relationship between the real and imaginary parts of a chiroptical response, which is mathematically described by the Kramers–Kronig integral relations. These relations allow the reconstruction of ORD from CD without direct ORD measurement, provided that the spectral data span a sufficiently broad and continuous range[3].

The Kramers–Kronig relations between CD and ORD are given by the following principal value integrals[4]:

$$\phi(\lambda) = \frac{2\lambda}{\pi}\mathcal{P}\int \frac{\theta(\mu)}{\mu^2 - \lambda^2}d\mu$$
$$\theta(\lambda) = -\frac{2\lambda}{\pi}\mathcal{P}\int \frac{\phi(\mu)}{\mu^2 - \lambda^2}d\mu \qquad (S1)$$

where $\theta(\lambda)$ and $\phi(\lambda)$ denote the CD and ORD spectra, respectively, and $\mathcal{P}$ indicates the Cauchy principal value. Since these integrals require knowledge of the optical response over an infinite spectral domain, a numerical approximation was implemented for practical application to finite datasets.

A symmetric, discrete approximation of the integral was used to perform the numerical transformation. The wavelength array was uniformly sampled with interval *h*, and the KK integrals were approximated as finite sums. Specifically, the ORD at each wavelength λ_i was calculated from the CD using the expression:

$$\phi(\lambda_i) \approx \frac{2h}{\pi}\lambda_i \sum_{j\neq i} \theta(\lambda_j)\frac{1}{\lambda_j^2 - \lambda_i^2} \qquad (S2)$$

To avoid divergence at $\lambda_i = \lambda_j$, a "leap-frog" method was applied[5]. This method selectively excludes the singularity by alternating the summation indices. For odd i, only even j are included in the summation, and vice versa. This approach significantly improves numerical stability while preserving the symmetry of the transformation.

After obtaining the ORD spectrum, the reversibility of the KK transformation was verified by performing an inverse transformation—computing CD from the calculated ORD using the corresponding discrete formula:

$$\theta(\lambda_i) \approx \frac{2h}{\pi}\lambda_i \sum_{j \neq i} \phi(\lambda_j) \frac{1}{\lambda_j^2 - \lambda_i^2} \qquad (S3)$$

The resulting CD spectrum displayed excellent agreement in shape with the original experimental data. However, a systematic vertical offset was observed, which arises due to the KK relation's inherent inability to capture constant (DC) components in the signal. To correct for this, a mean offset adjustment was applied, aligning the recovered CD with the original spectrum.

Supplementary Note 2: SHG electric field intensities for supertwisted WS_2 with twist angle is θ under left- and right- circular light

For a two-dimensional (2D) material with in-plane threefold rotation symmetry and mirror symmetry (For example: WS_2). Within the circular-polarization basis $\left(P_x = \varepsilon_0\chi^{(2)}\left(E_x^2 - E_y^2\right), P_x = -2\varepsilon_0\chi^{(2)}E_xE_y \Rightarrow P_- = \sqrt{2}\varepsilon_0\chi^{(2)}E_+^2, P_+ = \sqrt{2}\varepsilon_0\chi^{(2)}E_-^2\right)$ and under the slowly varying amplitude approximation, solving the nonlinear coupled-wave equations allows one to derive the twist-angle-dependent expression for nonlinear wave generation as follows:

$$\begin{cases} \boldsymbol{E}_{2\omega}^{-} = \dfrac{i\sqrt{2}\omega}{cn(2\omega)}\chi^{(2)}{\boldsymbol{E}_{\omega}^{+}}^2\displaystyle\int_0^T e^{-i[\Delta kz - 3\alpha(z)]}\,dz \\ \boldsymbol{E}_{2\omega}^{+} = \dfrac{i\sqrt{2}\omega}{cn(2\omega)}\chi^{(2)}{\boldsymbol{E}_{\omega}^{-}}^2\displaystyle\int_0^T e^{-i[\Delta kz + 3\alpha(z)]}\,dz \end{cases} \tag{S4}$$

where $\boldsymbol{E}_{2\omega}^{-}$, ($\boldsymbol{E}_{2\omega}^{+}$), and $\boldsymbol{E}_{\omega}^{-}$, ($\boldsymbol{E}_{\omega}^{+}$) are the left, (right) circularly polarized components of the second harmonic and fundamental waves, respectively, c is the speed of light in vacuum, $n(2\omega)$ is the refractive index of the second harmonic wave, $\Delta k = k_{2\omega} - 2k_{\omega}$ is the wavevector mismatch for SHG, $\alpha(z)$ is the twist angle of the layer at depth z. T is the total thickness of optical crystal.

When each layer of the WS_2 maintains a constant thickness and adjacent layers share the same twist angle θ, we can perform the following transformation on Equation (1), for the $(n+1)^{th}$ layer, its contribution to the electric field can be expressed as:

$$\boldsymbol{E}_{2\omega}^{\mp}(n+1) = \frac{i\sqrt{2}\omega}{cn(2\omega)}\chi^{(2)}{\boldsymbol{E}_{\omega}^{\pm}}^2\int_{nt}^{(n+1)t} e^{-i[\Delta kz \mp 3n\theta]}dz \tag{S5}$$

By integrating this segment, we obtain the following result:

$$\boldsymbol{E}_{2\omega}^{\mp}(n+1) = \frac{i\sqrt{2}\omega}{cn(2\omega)}\chi^{(2)}{\boldsymbol{E}_{\omega}^{\pm}}^2 \cdot e^{i3n\theta}\,\frac{e^{-i\Delta k(n+1)t} - e^{-i\Delta knt}}{-i\Delta k} \tag{S6}$$

By summing the contributions from all N layers and subsequently simplifying, we obtain:

$$
\begin{aligned}
\boldsymbol{E}_{2\omega}^{\mp} &= \frac{i\sqrt{2}\omega}{cn(2\omega)}\chi^{(2)}\boldsymbol{E}_{\omega}^{\pm\,2}\int_{0}^{Nt} e^{-i(\Delta kz\mp 3\theta)}dz \\
&= \frac{i\sqrt{2}\omega}{cn(2\omega)}\chi^{(2)}\boldsymbol{E}_{\omega}^{\pm\,2}\cdot\frac{e^{-i\Delta kt}-1}{-i\Delta k}\sum_{n=0}^{N} e^{-i(\Delta knz\mp 3\theta)} \\
&= \frac{i\sqrt{2}\omega}{cn(2\omega)}\chi^{(2)}\boldsymbol{E}_{\omega}^{\pm\,2}\cdot\frac{e^{-i\Delta kt}-1}{-i\Delta k}\cdot\frac{1-e^{-i\Delta kt}}{\Delta k}\cdot\frac{1-e^{-iN(\Delta kt\mp 3\theta)}}{1-e^{-i(\Delta kt\mp 3\theta)}}
\end{aligned}
\tag{S7}
$$

Supplementary References

1. Momma, K. & Izumi, F. VESTA 3 for three-dimensional visualization of crystal, volumetric and morphology data. *J. Appl. Cryst.* **44**, 1272-1276 (2011).
2. Munkhbat, B., Wróbel, P., Antosiewicz, T. J. & Shegai, T. O. Optical constants of several multilayer transition metal dichalcogenides measured by spectroscopic ellipsometry in the 300–1700 nm range: high index, anisotropy, and hyperbolicity. *ACS Photonics* **9**, 2398-2407 (2022).
3. Barron, L. D. *Molecular light scattering and optical activity*. 2 edn, (Cambridge University Press, 2004).
4. Emeis, C. A., Oosterhoff, L. J. & Vries, G. D. Numerical evaluation of Kramers—Kronig relations. *Proceedings of the Royal Society of London. A. Mathematical and Physical Sciences* **297**, 54-65 (1967).
5. Ohta, K. & Ishida, H. Comparison among several numerical integration methods for Kramers-Kronig transformation. *Appl. Spectrosc.* **42**, 952-957 (1988).